inorganics

MDPI

Article

C-TiO_2+Ni and ZnO+Ni Magnetic Photocatalyst Powder Synthesis by Reactive Magnetron Sputtering Technique and Their Application for Bacteria Inactivation

Martynas Lelis [1,*], Simona Tuckute [1], Marius Urbonavicius [1], Sarunas Varnagiris [1], Sandra Sakalauskaite [2] and Rimantas Daugelavicius [2]

[1] Center for Hydrogen Energy Technologies, Lithuanian Energy Institute, 3 Breslaujos St., 44403 Kaunas, Lithuania
[2] Department of Biochemistry, Faculty of Natural Sciences, Vytautas Magnus University, 44404 Kaunas, Lithuania
* Correspondence: martynas.lelis@lei.lt; Tel.: +370-37-401-904

Abstract: In the current study, a bi-layered magnetic photocatalyst powder consisting of a Ni layer on one side and carbon-doped TiO_2 or ZnO photocatalyst layers on the other side was synthesized by magnetron sputtering technique. SEM, XRD, and XPS analysis of powders revealed that the photocatalytic TiO_2 layer had a mixed anatase-rutile structure, was doped by carbon to approximately 3 at. % and had a fraction of Ti(III) oxide. Meanwhile, the ZnO layer was crystalized in a wurtzite structure and had a considerable number of intrinsic defects, which are useful for visible light photocatalysis. The activity of magnetic photocatalyst powder was tested by photocatalytic bleaching of dyes, as well as performing photocatalytic inactivation of *Salmonella* bacteria under UV and visible light irradiation. It was observed, that C-TiO_2+Ni magnetic photocatalyst had relatively high and stable activity under both light sources (for five consecutive cycles dye degradation reached approximately 95%), but ZnO+Ni was generally lacking in activity and stability (over five cycles under UV and visible light, dye degradation fell from approximately 60% to 55% and from 90% to 70%, respectively). Photocatalytic treatment of bacteria also provided mixed results. On one hand, in all tests bacteria were not inactivated completely. However, on the other hand, their susceptibility to antibiotics increased significantly.

Keywords: TiO_2; carbon doping; ZnO; magnetic photocatalyst; photocatalysis; repetitive cycling; heterostructure; water treatment; dye bleaching; bacteria inactivation

check for updates

Citation: Lelis, M.; Tuckute, S.; Urbonavicius, M.; Varnagiris, S.; Sakalauskaite, S.; Daugelavicius, R. C-TiO_2+Ni and ZnO+Ni Magnetic Photocatalyst Powder Synthesis by Reactive Magnetron Sputtering Technique and Their Application for Bacteria Inactivation. *Inorganics* **2023**, *11*, 59. https://doi.org/10.3390/inorganics11020059

Academic Editors: Franz Edwin López Suárez, Robison Buitrago and Andres F. Suárez

Received: 26 December 2022
Revised: 19 January 2023
Accepted: 24 January 2023
Published: 26 January 2023

1. Introduction

For decades, in most parts of the world, the issue of freshwater availability and its quality was either insignificant or inferior to the more prevailing concerns of economic growth, food affordability, and safety. Recently, these issues partially stepped down in actuality to more present-day topics like inflation, energy security, and climate change. Yet freshwater-related concerns remain peripheral. Despite this general public unawareness, the latest high-level reports [1–3] unequivocally stated that ongoing climate change is one of the central factors behind the shrinking availability of freshwater resources and the deterioration of their quality. Moreover, in 2021 the United Nations clearly signaled [2] that without proper measures, freshwater quality is doomed to deteriorate at an even faster rate. This prognosis may soon become imminent because global water consumption is increasing, but only half of the used water gets any treatment before it is released back into the ecosystem [2]. Naturally, to change this pernicious trend, societies have to change their behavior and lower water consumption. At the same time, wastewater [4,5], rainwater [6–8], and other commonly unused freshwater forms [9] have to be earnestly considered as valuable unexploited water resources. Unfortunately, most of these potentially usable water sources

usually possess significant levels of inorganic and/or organic pollutants, including dyes, pesticides, industrial by-products, effluents, pharmaceuticals, etc. [10]. In the same way, some of them are contaminated by biological pathogens such as *Salmonella* bacteria which can cause food-borne infections (gastroenteritis, fever, abdominal discomfort, nausea, and diarrhea) [11]. Accordingly, to make these water resources usable, a number of new up-to-date water cleaning facilities have to be installed, and the existing ones have to be upgraded to provide better cleaning, higher sustainability, and increased energy efficiency.

Currently, the most common water disinfection method is chlorination [12]. It provides satisfactory results, but scientists for years have pointed out its significant drawbacks, namely difficulties in completely removing residual-free chlorine and its toxic/cancerogenic residuals [12,13]. Besides, chlorine has insufficient efficiency against some microorganisms (bacteria, viruses, fungi, etc.) [10,14]. Accordingly, alternative disinfection technologies, such as ultraviolet, ozone, and photocatalytic disinfection were proposed.

Amongst them, photocatalytic disinfection stands out as probably the most complex, but at the same time potentially the most universal and the most efficient method. At its core, photocatalytic disinfection is a multi-step process, which uses a specific type of catalyst (commonly called photocatalysts), and ultraviolet (UV) or visible (Vis) light for the transformation of inert compounds (mostly H_2O and O_2 molecules) into reactive oxygen species (ROS), namely hydroxyl radicals (•OH), super oxide ions ($\cdot O_2^-$), peroxide (H_2O_2), singlet oxygen (O) and others [15]. ROS are very strong oxidizing and reducing agents. For example, the oxidative potential of •OH (2.8 V) and H_2O_2 (1.8 V) is considerably higher than chlorine (1.36 V) [16], therefore ROS are fully capable of universally degrading both chemical and biological pollutants. The important advantage of photocatalytically generated ROS over chlorine is their short life span (for example 4×10^{-9} s and 2×10^{-10} s for •OH and $\cdot O_2^-$, respectively [17]), which eliminates the need for the coercive ROS extraction or neutralization after the photocatalytic treatment procedure.

The key element of any decent photocatalytic water treatment process is the photocatalyst. Its properties fundamentally predetermine the limits for the ultimate efficiency of the photocatalytic cleaning process, whereas other parameters, such as light spectrum, irradiation intensity, photocatalyst/pollutant concentrations, and reactor design, arguably only define how much of this potential is exploited. A *good* photocatalyst is a semiconductor that is capable of efficiently absorbing UV and/or Vis light photons (by electron excitation from the valence to conduction band), generating electron (e^-) and hole (h^+) pairs, preventing charge recombination, and facilitating their diffusion to the surface. Next, in order to be suitable for ROS generation, e^- and h^+ have to be located at specifically positioned conduction and valence bands [18]. Finally, to meet up with the requirements of water cleaning facilities, photocatalysts have to be (i) biologically and chemically inert; (ii) maintain high photostability; (iii) be non-toxic, and (iv) cost-effective [19].

Up to now, considerable photocatalytic performance was observed with various forms of wide-bandgap metal oxides (TiO_2, ZnO, WO_3, Zn_2SO_4, Cu_2O, Fe_2O_3, $BiTiO_3$, etc.), sulfides (CdS, MoS_2, etc) and their heterostructures [18,20–23]. Among them, TiO_2-based materials stand out as the most extensively investigated and the mostly praised photocatalysts, with ZnO-based systems being one of the nearest runners-up. Metal and nonmetal doping [24–27], formation of heterostructures with other photocatalysts (p-n [28,29], surface [30], type-II [30,31], direct Z-scheme [32], S-scheme [33,34], Schottky junctions [35,36]) and different substrates [27,37–39], modification of photocatalyst particle size/shape [40,41], and other semiconductor engineering tools allowed obtaining photocatalysts whose efficiency surpassed pristine forms of TiO_2 and ZnO by some orders of magnitude, especially under visible light [42,43].

Altogether, progress in the enhancement of photocatalyst efficiency recently started to consolidate into stronger efforts to shift the research from the development of better photocatalysts towards the design and construction of pilot-scale reactors [44,45]. For practical applications, one of the key requirements is the ability to reuse the system and photocatalyst itself as many times as possible. Nanometric photocatalyst powder has an

exceptionally high surface area, which naturally translates into the highest ROS generation rates. However, the reusability of such powders is complicated, because it is very difficult to contain and/or recollect used nanoparticles [46,47]. Up to now, two solutions have been proposed. First, the photocatalyst is immobilized onto macroscopic sinking or floating substrates. This solution is relatively easy to implement and it is already applied in test reactors [44,45]. However, it has some serious drawbacks: i) immobilized photocatalyst loses a large fraction of its surface area, and ii) photocatalyst material is not homogeneously dispersed over the whole volume and overall photocatalytic cleaning efficiency falls remarkably. Second, photocatalyst materials can be combined with magnetic metals or compounds to form such called magnetic photocatalyst (MP) powder [48,49] which preserves a large specific surface area and can be evenly dispersed in the solution. At the same time, their magnetic properties allow using of magnetic fields (or ordinary magnets) for powder stirring, manipulation, and collection after usage [50]. On the whole, the MP concept is promising, but the development of MP materials is still relatively immature, and additional studies and testing are needed.

Another issue that is being faced at a pilot-scale application is the higher complexity of available pollutants. More specifically, due to convenience, up to now the largest share of laboratory tests were performed with the photocatalytic treatment of isolated inorganic compounds, however, real wastewater plants often have to deal with significant biological contamination and some biological species reacted to photocatalytic treatment in an unexpected manner. Accordingly, in recent years researchers started to conduct more photocatalytic disinfection tests with live microorganisms [51]. Studies with different bacteria (*S.* typhimurium, *E. coli*, *S. aureus*, *M. kansasii*, *M. avium*, etc.) and viruses (*MS2 bacteriophage*, Aerosol-Associated *Influenza*, *Norovirus (HuNoV)*, etc.) confirmed, that under favorable conditions, the photocatalytic inactivation rate can reach up to 100%. However, if conditions (temperature, pH, presence of other species) were not favorable, even for the same photocatalyst-pathogen pair, the inactivation rate could decrease radically [52]. Such results emphasized the fundamental difference between the treatment of inert objects (dyes, phenols, etc.) and much more complicated live objects (bacteria, viruses, etc.) that can respond to oxidative stress and mitigate the damage caused by ROS [53,54].

Considering the potential of MP materials, the scarcity of results on MP efficiency in dealing with live pathogens, and existing studies indicating that the actual effectiveness of any particular photocatalyst material strongly depends on its synthesis method [55], we decided to synthesize MP powder by atypically applied magnetron sputtering technique [56], and to test its suitability for the photocatalytic treatment of live bacteria. More specifically, the reactive magnetron sputtering technique was used to produce fine MP powder consisting of bi-layered particles having a well-proven photocatalyst (namely, carbon-doped TiO_2 [57] or zinc-rich ZnO [58,59]) on one side and ferromagnetic Ni metal layer on the other side. The activity of synthesized MP powder was tested by photocatalytic inactivation of *Salmonella* typhimurium bacteria under UV and visible light.

2. Results and Discussions

2.1. Characterization of C-TiO_2+Ni and ZnO+Ni MP Structure

In the current study, TiO_2 and ZnO-based MP powders were synthesized by following a three-step procedure (full details are provided in Section 3). First, conventional magnetron sputtering in an inert Ar gas atmosphere was used to deposit a metallic Ni layer on salt grains. Second, the selected photocatalyst film (C-TiO_2 or zinc-rich ZnO) was deposited on top of the first layer by reactive magnetron sputtering in the Ar-O_2 gas mixture. Third, salt grains with bi-layered coatings were poured into distilled water. By applying gentle stirring, the salt was quickly dissolved and solid particles were released. Repetitive rinsing with fresh water was applied to carefully wash off any salt residuals from the particles. Lastly, the particles were sedimented, collected, and dried out for 48 h in an ambient atmosphere. Based on the used photocatalyst layer (i.e., carbon doped TiO_2, or ZnO) in the following text the bi-layered MP powders are named as C-TiO_2+Ni and ZnO+Ni.

To achieve higher TiO_2 phase crystallinity and higher photocatalytic activity of carbon-doped titania, C-TiO_2+Ni MP powder was calcinated at 450 °C for 2 h (the benefits of TiO_2 powder calcination were previously discussed at [60,61]). In the case of ZnO, we wanted to preserve the as-received wurtzite structure with a significant number of intrinsic defects, namely zinc interstitials (Zn_i) and oxygen vacancies (V_O) (more details on intrinsic ZnO defects can be found at [62]). Therefore, the calcination step for ZnO+Ni powder was not applied.

SEM images of typical washed-off C-TiO_2+Ni and ZnO+Ni MP powder particles are presented in Figure 1a,b, respectively. The images reveal, that washed-off particles can be characterized as thin shells reaching 200–300 µm in diameter, which can be altered by choosing differently sized salt grains [56]. EDS elemental maps (Figure 1c–f) clearly confirmed the bi-layered structure for both MP powders. The internal side of the shells was dominated by nickel (green color), whereas outer shells were composed of oxygen (blue) and titanium or zinc (both marked in red color) for C-TiO_2+Ni and ZnO+Ni MP powder, respectively.

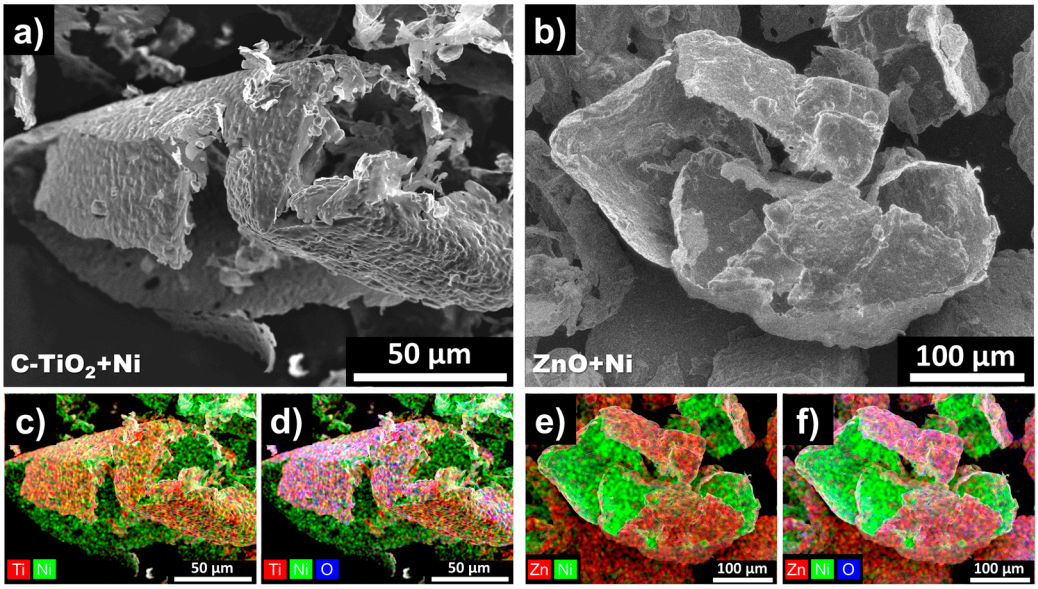

Figure 1. SEM images and EDS elemental maps of typical MP particles: (**a**) SEM image of C-TiO_2+Ni; (**b**) SEM image of ZnO+Ni; (**c**) elemental map of C-TiO_2+Ni excluding oxygen; (**d**) elemental map of C-TiO_2+Ni including oxygen; (**e**) elemental map of ZnO+Ni excluding oxygen; (**f**) elemental map of ZnO+Ni including oxygen. Red color represents Ti and Zn, green represents nickel, and blue represents oxygen. In images (**d**,**f**) pink color regions are the result of an additive mixing of red and blue colors, therefore pink can be considered as the representative of C-TiO_2 and ZnO photocatalysts distribution.

XRD analysis of C-TiO_2+Ni powder (Figure 2) supplements EDS results and reveals that carbon-doped TiO_2 crystallized into anatase (tetragonal, space group $I4_1/amd$) and rutile (tetragonal, space group $P4_2/mnm$) phases at an approximate ratio of 2:1. The average crystallite size of the anatase and rutile phase TiO_2 reached 28.2 nm and 16.3 nm, respectively. In addition to titania, two nickel-containing phases were observed, namely cubic Ni (space group Fm-3m) and rhombohedral NiO (space group R-3m). NiO was identified at the pattern of the calcinated C-TiO_2+Ni MP powder only, but it was not observed for any other as-deposited MP powder (including ZnO+Ni). Accordingly, NiO formation was ascribed solely to the calcination step. It is interesting to note, that the most typical form of NiO synthesized by chemical methods is the paramagnetic NaCl type cubic phase. However, in calcinated C-TiO_2+Ni MP powder, an antiferromagnetic rhombohedral NiO cell (generally considered as a distorted cubic phase [63–65]) was identified. The later

form of NiO was previously observed in other magnetron sputter-deposited films [65]. Recently, both first-principles calculations and model simulations showed that this cubic-rhombohedral phase transition is caused by a particular magnetic arrangement [64] which is evidently realized by the magnetron sputtering technique.

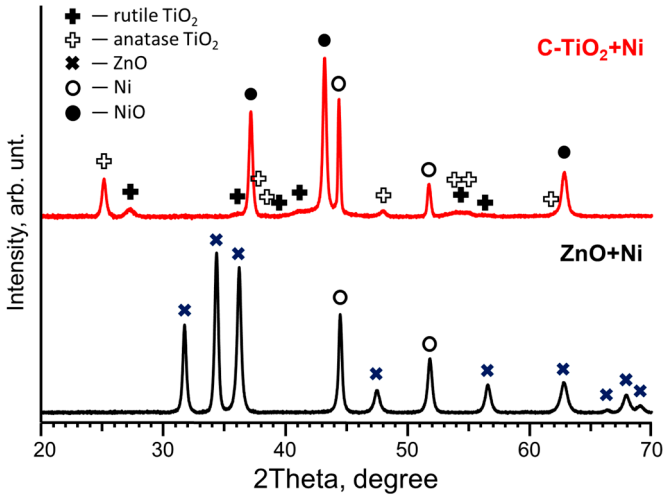

Figure 2. XRD patterns of C-TiO_2+Ni (red) and ZnO+Ni (black) MP powder.

To confirm that the TiO_2 phase was actually doped by carbon, we analyzed its composition and structure by XPS technique (Figure 3). Elemental composition at the surface was 26.4 at. % Ti, 62.5 at. % O, and 9.9 at. % C. During preparation, samples were carried out in ambient air, therefore surface composition was evidently affected by the adventitious contamination and adsorption of water moisture. Naturally, this is reflected in increased concentrations of C and O. To have a better understanding of a bulk composition, we measured the composition of the pre-sputtered sample and estimated it at 34.4 at. %, 62.5 at. %, and 3.1 at. %, for Ti, O, and C,, respectively. Later composition is a good representation of the carbon-doped TiO_2 with some degree of oxygen vacancies.

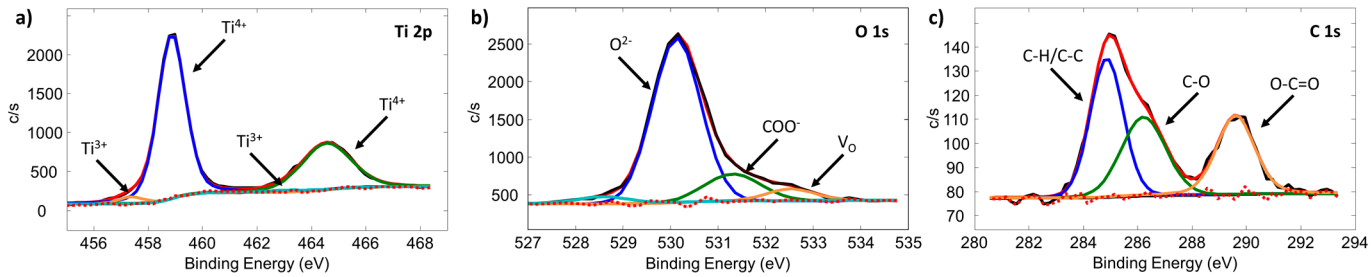

Figure 3. High-resolution XPS spectra of C-TiO_2 photocatalyst layer: (**a**) Ti 2p; (**b**) O 1s; and (**c**) C 1s.

Ti $2p_{3/2}$ and Ti $2p_{1/2}$ spin-orbital doublet peaks (at approximately 459 eV and 464.5 eV, respectively) were fitted by two titanium chemical states. The main Ti $2p_{3/2}$ peak at 458.8 eV was ascribed to the TiO_2 phase. Its binding energy is slightly higher than the reference TiO_2 value but is equal to the value observed for the TiO_2 samples with oxygen vacancies [66]. The presence of oxygen vacancies and/or distortion caused by carbon doping is also evident by the observation of a smaller peak at 457.4 eV, which is attributed to the Ti^{3+} state [66]. We presume that the contribution of the Ti^{3+} state is relatively low (the area ratio of Ti^{3+} and Ti^{4+} peaks is approximately 3.5:96.5) because the lack of some Ti-O bonds is compensated by partial titanium bonding directly to carbonaceous species. This is supported by O 1s and C 1s spectra (Figure 3b,c, respectively), which indicate, that in addition to peaks ascribed to O^{2-} anions in crystalline titanium dioxide (530.1 eV) and graphitic carbon (284.8 eV), there are at least four additional peaks. As discussed by L. Zhang et al. [66] and P. Zabek et al. [67], O 1s

peaks at 531.3 eV and 532.5 eV are attributed to carboxylate groups and oxygen vacancies, though they also can be contributed to by some surface hydroxyl groups and water moisture adsorbed from the atmosphere. C 1s spectra apart from the C-C/C-H peak at 284.8 eV also contain peaks at 286.2 eV and 289.6 eV which are attributed to the C-O and O-C=O groups, respectively [68]. While some fraction of C-C/C-H and C-O can be arguably ascribed to the adventitious sample contamination in air, the observance of the O-C=O peak and presence of carbon in the pre-sputtered sample make up non-disputable evidence of successful carbon doping in the TiO_2 photocatalyst layer.

To sum up the structural analysis of the C-TiO_2 layer we can note a few things. First, the C-TiO_2 layer consists of a mixture of rutile and anatase phases. Naturally, between the dissimilar domains, there are some mismatches and they potentially disturb atom arrangements at the boundaries. Second, XPS analysis demonstrated that a) titanium oxide is doped by approximately 3 at. % of carbon; b) there is up to 4% of titanium in the Ti^{3+} chemical state; and c) approximately one quarter of the oxygen can be attributed to carboxylate groups and oxygen vacancies. Altogether, this demonstrates that the C-TiO_2 layer has a significant concentration of various defects which can be useful for the photocatalytic efficiency (more details on the positive effect of rutile-anatase phase mixing can be found at [69,70], for oxygen vacancies and Ti^{3+} at [71–73], and for carbon doping at [74,75]).

XRD pattern of ZnO+Ni MP powder (Figure 2) had peaks from two phases: hexagonal wurtzite ZnO (space group $P6_3mc$) and cubic metallic Ni (space group Fm-3m). On one hand, at ambient conditions, the wurtzite structure is the most stable ZnO phase and is typically observed for nearly all ZnO films formed by reactive magnetron sputtering as well as for most ZnO powder formed by wet chemical methods [76–82]. On the other hand, wurtzite phase ZnO is also well known for its tendency to naturally include high levels of various intrinsic defects. V_O and Zn_i were already mentioned above, but other defects, like oxygen interstitials (O_i) and zinc vacancies (V_{Zn}), can be present as well [83]. Intrinsic ZnO defects create intermediate electron energy levels and at certain concentrations can significantly enhance the absorption of visible light and facilitate e^--h^+ pairs separation [84]. Accordingly, the presence of specific intrinsic defects can have a severe impact on the photocatalytic performance of the ZnO photocatalyst.

In our previous studies [59,85], we demonstrated that particularly efficient orange-red colored ZnO photocatalyst films were obtained when reactive magnetron sputtering of zinc was performed in an oxygen-poor Ar-O_2 working gas mixture. The characteristic orange-red color is very unusual for the traditional un-doped ZnO, thus its presence serves as reliable optical evidence of a high concentration of Zn_i and V_O defects [59,86]. Accordingly, in the current study, ZnO+Ni photocatalyst layer deposition parameters were optimized to obtain orange-red colored zinc-rich ZnO films with a similar structure as declared in [59,85].

The elemental composition analysis by XPS confirmed that parameters optimization was successful and Zn rich ZnO layer composition was: Zn: 50.4 at. %, O: 43.2 at %, and C: 6.4 at. %. To verify the existence of Zn_i and V_O defects, we used the XPS instrument to measure high-resolution spectra of Zn 2p and O 1s photoelectrons (Figure 4a,b, respectively), as well as Zn LMM Auger electrons (Figure 4c). The acquired Zn 2p spectra had highly symmetrical Zn $2p_{3/2}$ and Zn $2p_{1/2}$ peaks, which were fitted by two components correspondingly centered at 1021.8 eV and 1044.8 eV. The observed binding energy of the Zn $2p_{3/2}$ peak can be attributed to the ZnO phase, but the Zn 2p binding energy shift (in comparison to Zn metal) for different zinc compounds is small [87], therefore chemical state identification solely by Zn 2p spectra is not credible. For instance, Zn $2p_{3/2}$ peaks for Zn and ZnO usually are positioned in the same narrow range between 1021.7–1022.0 eV [87]. Accordingly, there is a chance that the presumable ZnO phase peak is overlapped by the photoelectrons coming from Zn_i or some other zinc domain.

Luckily, O 1s and Zn LMM peaks are more sensitive to the presence of ZnO defects and they allow us to get a better understanding of the chemical composition of the ZnO layer. O 1s envelope was fitted by three peaks centered at 530.4 eV, 531.2 eV, and 532.4 eV. In such a configuration, the lowest binding energy peak is typically ascribed to the O^{2-}

ions within the stoichiometric hexagonal wurtzite structure [88–90]. The middle peak is attributed to the O^{2-} ions in oxygen-deficient ZnO regions (for example next to the V_O or Zn_i), whereas the largest binding energy peak is usually produced by the loosely bound surface oxygen (for example adsorbed moisture or carbon oxide) [88–90]. Comparison of relative O 1s spectra component areas (69.2%, 16.9%, and 13.9%) allows us to estimate that defect concentration in the ZnO layer was relatively high—approximately every fourth or fifth oxygen atom (ion) was neighboring oxygen vacancy, zinc interstitial or some other oxygen-deficient irregularity.

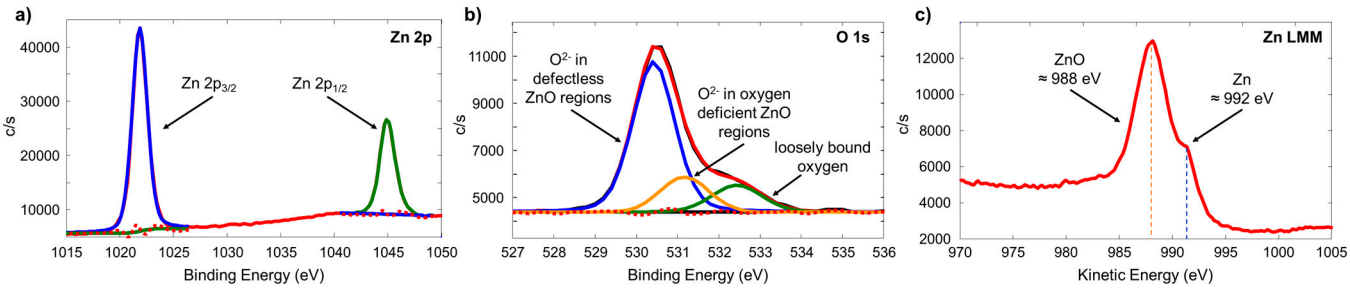

Figure 4. High-resolution XPS spectra of ZnO photocatalyst layer: (**a**) Zn 2p, (**b**) Zn LMM, and (**c**) O 1s.

2.2. Estimation of C-TiO$_2$+Ni and ZnO+Ni MP Photocatalytic Activity

Before proceeding to the photocatalytic disinfection of *Salmonella* Typhimurium we tested both MPs for the repetitive bleaching of Methylene blue solution under UV light and Rhodamine B solution under Vis light irradiation (Figure 5). The observed data showed that C-TiO+Ni were capable of constantly delivering approximately 95% dye concentration reduction under both light sources. Whereas, ZnO+Ni had a considerably lower reduction of dye concentrations, especially under UV light. Moreover, ZnO+Ni showed a degrading trend of photocatalyst activity. As will be discussed below, this reduction is attributed to the partial dissolution of Zn and consequent degradation of the intrinsically modified ZnO structure.

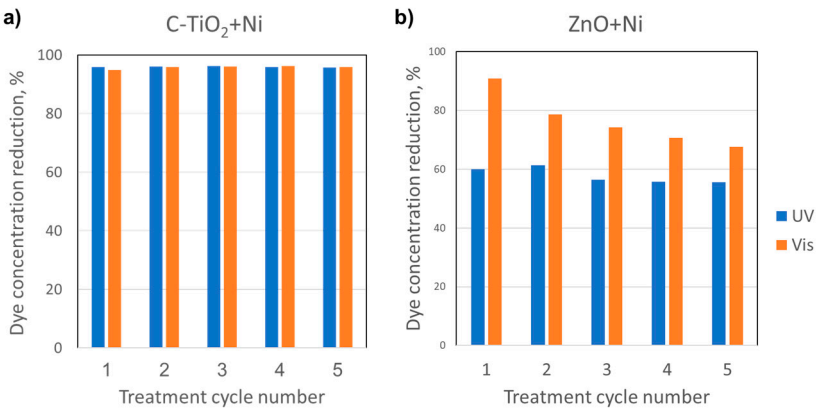

Figure 5. Repetitive photocatalytic bleaching of Methylene blue solution under UV light and Rhodamine B solution under Vis light irradiation: (**a**) bleaching using C-TiO$_2$+Ni photocatalyst, (**b**) bleaching using ZnO+Ni photocatalyst.

2.2.1. Photocatalytic *S.* Typhimurium Bacteria Disinfection with C-TiO$_2$+Ni MP

To evaluate the photocatalytic efficiency of C-TiO$_2$+Ni and ZnO+Ni MP powders, we used them for the treatment of *Salmonella* Typhimurium bacteria under ultraviolet (UV) and visible (Vis) light irradiation. During these experiments, two control groups of unlit *S.* Typhimurium bacteria were used. The first control group (CG I) consisted of *S.* Typhimurium bacteria which were kept in the dark (stirred and thermostated) without any additional factor. Meanwhile, the second control group (CG II) was equally kept in the dark, but this time selected MP powder was added to the solution.

S. Typhimurium bacteria plating and cultivation on agar plates showed, that in the dark, C-TiO_2+Ni powder increases cells' capability to form colonies by 9.2% (Figure 6). Detailed analysis of the specific mechanism of how C-TiO_2+Ni powder stimulates the growth of *S.* Typhimurium bacteria colonies was not a part of this study and remains disputable. Nevertheless, some deductions on key acting factors can be made. First, earlier reports [53] demonstrated, that a similarly sized (approximately 10%) positive effect of undoped TiO_2 on *S.* Typhimurium bacteria viability was also observed when the same bacteria were treated by standardized commercial P25 Degussa TiO_2 powder. Second, ZnO+Ni MP did not have a positive effect on the bacteria's ability to form colonies (more details are provided in Section 2.2.2). Based on these facts, it is assumed that *S.* Typhimurium viability stimulation is the specific feature of TiO_2 itself, rather than an effect of Ni or an outcome of a more complex interaction with whole C-TiO_2+Ni particles. Thereby, it is also presumed that the Ni layer does not have a significant effect on the *S.* Typhimurium bacteria's capability to form new colonies.

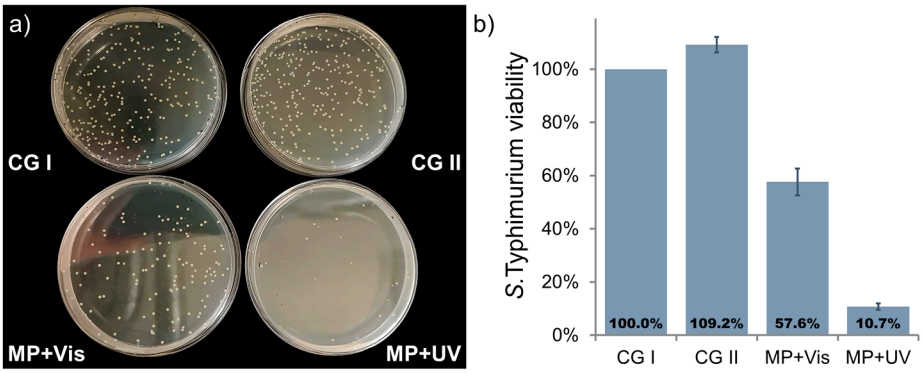

Figure 6. Results of *S.* Typhimurium bacteria plating and cultivation on agar plates after they were treated with C-TiO_2+Ni MP powder under visible (MP+Vis) and UV (MP+UV) light irradiation: (**a**) qualitative representation, and (**b**) averaged quantitative estimation. Two *S.* Typhimurium control groups (CG I without MP and CG II with MP) were maintained in the dark to determine the base values of bacteria viability.

After photocatalytic *S.* Typhimurium treatment under Vis and UV light, their viability was reduced by approximately 40% and 90%, respectively (Figure 6b). Naturally, the direct comparison of C-TiO_2+Ni efficiency to the performance of other magnetic photocatalysts is not appropriate, because most of the researchers use different probing objects (bacteria, dyes, pesticides, etc.) and testing methodologies. Still, it can be implied, that observed MP activity is at least moderate, because similar *S.* Typhimurium bacteria treatment by P25 TiO_2 powder and visible light reduced *S.* Typhimurium viability by approximately 2–3% [53], whereas under UV light in 1 h P25 TiO_2 reduced bacteria viability by approximately 22% [53].

Earlier reports have demonstrated that usually photocatalytic treatment of gram-negative bacteria first damages its outer membrane and opens up the path to attack the cytoplasmic membrane [91]. Eventually, the loss of cytoplasmic membrane integrity leads to the death of the cells. Data in Figure 6 showed that during photocatalytic treatment, not all bacteria cells suffered lethal damage. Nevertheless, it can be assumed that most of them were affected and we wanted to obtain a more accurate estimate of this damage level. Hence, we measured how unaffected and photocatalytically treated *S.* Typhimurium bacteria uptake N-phenyl-1-naphthylamine (NPN). NPN is a hydrophobic fluorescent probe whose fluorescence increases remarkably in a hydrophobic environment (e.g., membrane lipid bilayer). Accordingly, its uptake can be used to assess the permeability of the gram-negative bacteria membrane [53].

NPN uptake data (Figure 7) shows that C-TiO_2+Ni MP alone (CG II) had only a limited effect on the permeability of the *S.* Typhimurium membrane. After photocatalytic treatment with photocatalyst under Vis (MP-Vis) and UV (MP-UV) light, the permeability

of the bacteria membrane was increased by approximately 40% and 50%, respectively. The increase was statistically significant; however, it was approximately two times lower than the almost 95% increase for the fully permeabilized membrane (PMB sample represents *S*. Typhimurium bacteria treated by polymyxin B antibiotic which is highly efficient against these Gram-negative bacteria).

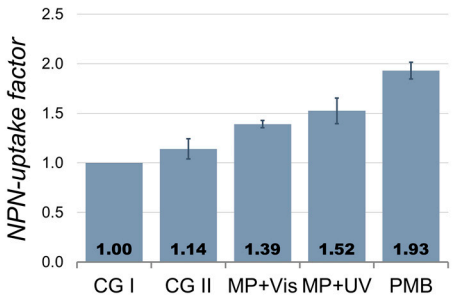

Figure 7. Effects of light and C-TiO_2+Ni MP powder on *S*. Typhimurium outer membrane permeability. Two control groups represent data for *S*. Typhimurium bacteria which were maintained in the dark without (CG I) and with (CG II) C-TiO_2+Ni MP powder, respectively. MP+Vis and MP+UV samples correspondingly show measures obtained with C-TiO_2+Ni MP powder and Vis or UV light. PMB samples (bacteria treated by polymyxin B) were used as the additional control for fully permeabilized bacteria membranes.

The NPN uptake results confirmed that even when photocatalytic treatment does not fully inactivate *S*. Typhimurium cells, it is still capable of inducing significant changes in membrane permeability. Partial permeabilization of membranes opens up a path for external ROS to enter the cell and cause direct damage to bacteria DNA/protein (Figure 8). However, this direct mechanism is not the only one which can cause the death of the cell. For instance, in addition to leaking photocatalytically generated ROS, the permeabilized membrane can also transmit other substances from the solution to the cell. For example, these substances can be ultra-fine nanometric photocatalyst particles, dissolved salts (for example constituents of pH buffer), or other additives like NPN which we used to assess the membrane permeability [92]. In metabolizing bacteria, some of these substances can initiate the generation of internal ROS and induce internal oxidative stress which adds up to the direct damage caused by external ROS [53]. Similarly, even partial disruption of the cell membrane can lead to the leakage of DNA fragments and/or K^- ions from the cell to the solution. These secondary processes contribute to the bactericidal effect of photocatalytic treatment and allow the achievement of up to 90% inactivation (Figure 6), even though *S*. Typhimurium membrane permeabilization was just halfway to its full disruption (Figure 7).

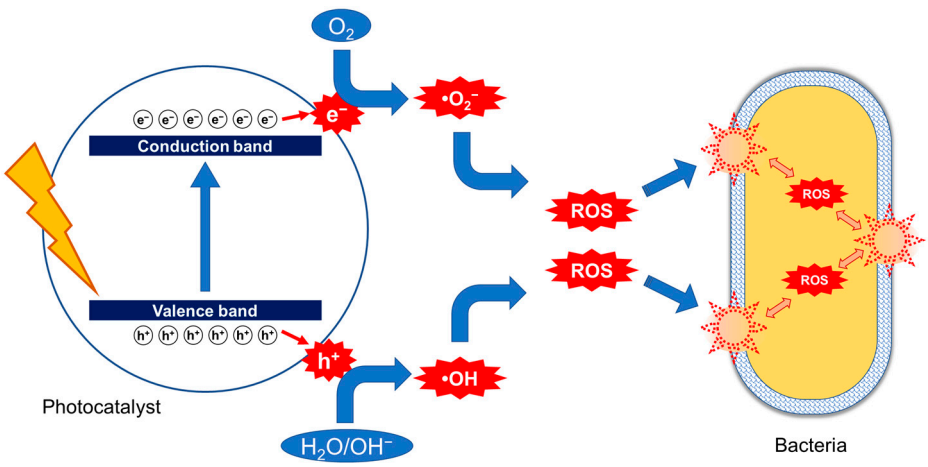

Figure 8. Schematic illustration of photocatalytic *S*. Typhimurium bacteria inactivation mechanism.

Naturally, for practical disinfection bacteria viability reduction by 40 or even 90 percent can be not sufficient. Nevertheless, significant permeabilization of bacteria membranes potentially still can be very useful. More specifically, photocatalytic pre-treatment of bacteria can be used to lower their susceptibility to traditional drugs and can be especially beneficial for solutions containing antibiotic-resistant bacteria. To check how the applied treatment with C-TiO_2+Ni powder affects bacteria response to the selected antibiotics, we determined the minimal inhibitory concentration (MIC) values of tetracycline and chloramphenicol drugs.

The obtained results (Table 1) revealed that for tetracycline MIC_{50} values decreased after all types of applied treatment. However, MIC_{90} values remained unchanged, stressing the difficulty to achieve full inactivation of bacteria. On the other hand, using chloramphenicol, photocatalytic treatment of bacteria under Vis and UV light decreased MIC_{50} value nearly two times. A similar reduction was observed for the MIC_{90} value measured for the bacteria treated by C-TiO_2+Ni powder under UV light, but other MIC_{90} values remained unchanged.

Table 1. The susceptibility of bacteria cells to antibiotics before and after treatment with C-TiO_2+Ni.

	Tetracycline, μg/mL		**Chloramphenicol, μg/mL**	
	MIC_{50} *	**MIC_{90} ***	**MIC_{50} ***	**MIC_{90} ***
CG I	1.2	2	3.5	8
CG II	**0.8**	2	3.5	8
MP+Vis	**0.8**	2	**1.8**	8
MP+UV	**0.5**	2	**2.2**	**4**

* MIC_{50} and MIC_{90} correspondingly represent the minimal antibiotic amount that is needed to inactivate 50% and 90% of initial bacteria.

2.2.2. Photocatalytic *S.* Typhimurium Bacteria Disinfection with ZnO+Ni MP

S. Typhimurium bacteria treatment with ZnO+Ni powder produced significantly different results. First, it can be noted that ZnO+Ni powder alone reduced bacteria viability by more than 40% (Figure 9). Furthermore, photocatalyst activity under Vis light was poor and had no effect on the bacteria's capability to form colonies. However, its activity under UV light was strong and nearly all bacteria were inactivated. We assume that such results were mostly influenced by the lower inertness of the ZnO-Ni photocatalyst. More specifically, it is known that depending on the synthesis method, ZnO has a weaker or stronger tendency to partially dissolve up to the pH of 10 [93,94]. Accordingly, Zn^{2+} ions enter into the solution, directly interact with *S.* Typhimurium bacteria, enter into the bacteria cell, and subsequently reduce its viability [94].

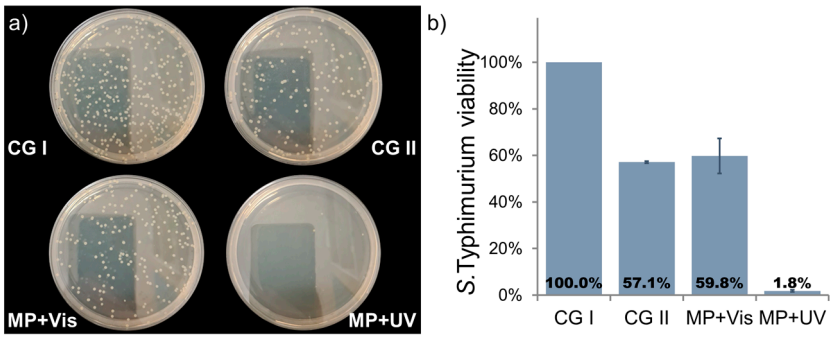

Figure 9. Results of *S.* Typhimurium bacteria plating and cultivation on agar plates after they were treated with ZnO+Ni MP powder under visible (MP+Vis) and UV (MP+UV) light irradiation: (**a**) qualitative representation and (**b**) averaged quantitative estimation. Two *S.* Typhimurium control groups (CG I without MP and CG II with MP) were maintained in the dark to determine the base values of bacteria viability.

NPN-uptake factors for *S.* Typhimurium treated with ZnO+Ni powder (Figure 10) complements the results of bacteria viability and shows, that generally all treatment methods had limited effect on cell membrane permeability. Accordingly, this indicates, that bacteria disinfection by ZnO+Ni powder relies slightly on other mechanisms than was the case of C-TiO_2+Ni [94]. Nevertheless, the dissolution of Zn^{2+} ions and their direct interaction with bacteria cells leads to a significant reduction of MIC values (Table 2), which even surpass the corresponding values obtained for bacteria treated with C-TiO_2+Ni (Table 1).

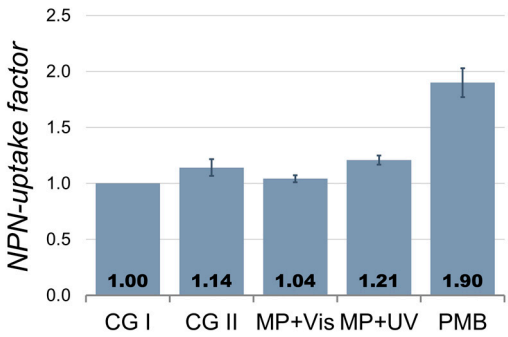

Figure 10. Effects of light and ZnO+Ni MP powder on *S.* Typhimurium outer membrane permeability. Two control groups represent data for *S.* Typhimurium bacteria which were maintained in the dark without (CG I) and with (CG II) ZnO+Ni MP powder, respectively. MP+Vis and MP+UV samples correspondingly show measures obtained with ZnO+Ni MP powder and Vis or UV light. PMB samples (bacteria treated by polymyxin B) were used as the additional control for fully permeabilized bacteria membranes.

Table 2. The susceptibility of bacteria cells to antibiotics before and after treatment with ZnO+Ni.

	Tetracycline, µg/mL		Chloramphenicol, µg/mL	
	MIC_{50} *	MIC_{90} *	MIC_{50} *	MIC_{90} *
CG I	1	2	3	8
CG II	**0.7**	2	3	8
MP+Vis	**0.7**	2	**3**	8
MP+UV	**0.4**	**1**	**1**	**4**

* MIC_{50} and MIC_{90} correspondingly represent the minimal antibiotic amount that is needed to inactivate 50% and 90% of initial bacteria.

3. Materials and Methods

3.1. Magnetic Photocatalyst Synthesis

Bi-layered photocatalyst powder synthesis was conducted by three-step procedure. First, fine K_2SO_4 salt grains were covered up by thin Ni layer. This ferromagnetic metal was used to provide magnetic properties for the photocatalyst particles. Then second layer consisting of active photocatalyst material, namely carbon-doped titanium dioxide (C-TiO_2) or zinc oxide (ZnO), was deposited on top of Ni. During the third step, coated salt grains were poured into glass vessel filled up with distilled water. In water, the salt dissolved and released solid bi-layered magnetic photocatalyst particles which were sedimented at the bottom of the vessel. Obtained MP particles were thoroughly washed off by repetitive rinsing with distilled water. After approximately ten rinsing rounds, water was fully drained off and remaining bi-layered powders were dried up for 48 h at room temperature. Ultimately, to achieve stronger crystallization of TiO_2 phase, MP powders were calcinated for 2 h at 450 °C.

Deposition of Ni and photocatalyst layers was conducted at K.J. Lesker PVD-75 (Jefferson Hills, PA, USA) vacuum system equipped with 76 mm diameter Torrus 3 unbalanced magnetrons. The distance between K_2SO_4 grains and Ni target (76 mm diameter, 99.99% purity) was approximately 35 mm. During Ni deposition selected unbalanced magnetron was operated at a constant 300 W rate supplied by DC power source. After initial 5 min

target pre-sputtering (cleaning with closed shutter), actual Ni deposition process proceeded for 3 min in inert Ar gas atmosphere (total pressure 0.6 Pa, gas purity 99.999%).

In our previous study [56], we demonstrated that by applying similar conditions for Ni deposition on salt grains and later washing the salt off to obtain free-standing Ni powder, we obtain powder with a magnetization value of 33–44 emu/g. In comparison, the reported magnetization values for carbon-doped TiO_2 and ZnO materials mostly did not exceed 0.01 emu/g [95–97]. Besides the evident benefit in providing magnetic properties for the MP, formation of bi-layered C-TiO_2+Ni and ZnO+Ni heterostructures also can be viewed as the enhancers of the photocatalytic performance of C-TiO_2 and ZnO photocatalyst. For instance, comparison of photocatalytic performance of corresponding photocatalysts on flat borosilicate glass and floating HDPE grains showed that provision of Ni underlayer improved photocatalyst performance by 20–30% [52,85]. Comparable results were also reported by I. Limon-Rocha et al. [98] who used small quantities of Ni to decorate nanometric TiO_2 powder produced by chemical methods.

For C-TiO_2 photocatalyst layer deposition magnetron was equipped with high purity (99.99%) Ti target with embedded graphite pieces. The ratio of exposed titanium and carbon surface areas was approximately 1:1. C-TiO_2 film deposition was performed using Ar-O_2 gas mixture at a total pressure of 0.66 Pa (Ar:O_2 gas supply ratio was approximately 3.6:1). The distance between the sample holder and Ti target was maintained at 35 mm. Typically for the most reactive metals, titanium sputtering in oxygen-containing atmosphere is a considerably slower and more complex process when a relatively plain deposition of Ni in inert Ar atmosphere. Accordingly, to obtain approximately 1 micrometer thick C-TiO_2 films, the deposition time was increased up to 2 h, magnetron power 400W. Furthermore, to improve reactive magnetron sputtering process stability and to maintain satisfactory sputtering rate C-TiO_2 of layer, the deposition was conducted using pulsed-DC power source (advantages of pulsed-DC power source are described at [99–101]). In comparison to un-doped TiO_2 films, optical transparency of C-TiO_2 films deposited using current method was significantly lower (approximately 90% for TiO_2 versus 20–40% for C-TiO_2), similarly, band gap value of C-TiO_2 was 3.1 eV, while for TiO_2 film it was 3.26 eV [102].

ZnO photocatalyst layer was deposited using the same magnetron sputtering system as for C-TiO_2. An unbalanced magnetron with a circular Zn target (99.99% purity and 76 mm diameter) was powered by an RF power source working at 150 W for 1 h. The distance between sample and Zn target was approximately 7 cm. The ZnO film was deposited at a fixed pressure of 1×10^{-2} mbar which was preselected experimentally as an optimal one according to our previous study [85]. The approximate thickness of ZnO layer was 4–5 µm. While using the same method for the deposition of ZnO films on flat borosilicate glass wafers we found that orange-red color ZnO film at 700 nm had a transparency of approximately 80%, but moving to the lower wavelengths, transparencyfell down continuously to nearly 0% just below the 400 nm mark [59]. The band gap value for such ZnO film was estimated at approximately 3.08 eV. In comparison, the *traditional* ZnO film without intentional oxygen deficit had a nearly linear transparency of 90% over all visible light spectra, and its band gap was estimated at 3.22 eV [59].

3.2. Characterization

3.2.1. Structure Analysis

Crystal structure of MPs was characterized by x-ray diffraction method. The diffraction data were acquired using Bruker D8 (XRD, Bruker D8, Hamburg, Germany) instrument with Cu Kα radiation working in Theta-Theta modification. Particle size and morphology changes were observed by Scanning Electron Microscope (SEM, Hitachi S-3400N, Tokyo, Japan). Elemental maps of the samples were acquired by energy dispersive spectrometer (Bruker Quad 5040, Hamburg, Germany), which was attached to the above-mentioned SEM. Chemical state of elements inside photocatalyst layer were characterized using X-ray Photoelectron Spectrometer (XPS, Versaprobe 5000, PHI, USA). For these measurements samples were deposited on flat glass wafers. During spectra acquisition, dual charge

neutralization by low-energy Ar^+ ions and electrons was applied. Before peak fitting by Multipak software, all spectra were shifted to have an adventitious carbon C 1s peak at 284.8 eV.

3.2.2. Repetitive Photocatalytic Bleaching of Dyes

The first photocatalytic activity of synthesized samples was tested using repetitive photocatalytic bleaching of aqueous Methylene blue (MB) and Rhodamine B (RhB) solutions. Photocatalytic bleaching experiments were performed in a round bottom quartz crucible (50 mm top diameter) which was fixed onto thermostatic base (22 °C) and was covered up by thin fused silica wafer (more than 90% transmission over whole 200–2000 nm spectral range). Thorlabs SOLIS-3C (5700 K, Thorlabs, Dachau, Germany) High-Power daylight white LED unit working at 90% of its nominal capacity (irradiation intensity at the solution surface of approximately 230 mW/cm^2) was used as a visible light source. The intensity of UV light source (Thorlabs M365LP1-C5) at the surface of reaction solution was 23.5 mW/cm^2 (Thorlabs, Dachau, Germany). The total MB/RhB volume was 10 mL, and dye concentration was 10 mg/ml. The magnetic stirring bar was added to the solution. During photocatalytic treatment experiments, powder samples (initial amount was 45 mg) were stirred continuously at 700 rpm. The stirring was only temporarily paused (for 2 min) before each intermediate (every 30 min) and final (total time 3 h) specimen collection. At the periods when the stirring was switched off, magnetic photocatalyst particles rapidly reacted to the magnetic field of the stirring bar and readily agglomerated at its surface. This feature was exploited for both collecting powder-free MB/RhB solution samples for the measurements of remaining dye concentrations (by UV-Vis light spectrometer (Jasco V-650, Tokyo, Japan)), and for the change of the MB/RhB solution between the consecutive cycles of the repetitive powder applications.

3.2.3. Photocatalytic Bacteria Inactivation

Gram-negative *Salmonella enterica* subsp. *enterica* serovar Typhimurium SL1344 cells were obtained from Prof. Séamus Fanning (Institute of Food and Health, University College Dublin, Ireland). Bacteria suspensions for the treatment were prepared as described in [85]. The treatment of bacteria was carried out in 15 mL of phosphate-buffered saline (PBS) solution pH 7.4 (Roth, Karlsruhe, Germany) in thermostated vessels with stirring (333 rpm) at 22 °C. C-TiO2+Ni and ZnO+Ni powder were kept in the dark before the experiment. The amount of inoculated S. Typhimurium bacteria was 3×10^4 cfu/ml. The duration of the irradiation was 2.5 h when Vis light and UV light intensities were 70 mW/cm^2 (1.35 A) and 30 mW/cm^2, respectively.

For viability test after 2.5 h of the treatment, 1 mL of sample suspensions were collected from the test cuvettes, diluted ten times, and 100 µL of obtained suspension was plated on LB agar (spread plate (SP) method with glass beads technique, named Copacabana Method [53]). The colonies formed were enumerated after incubating the plates at 37 °C for 18–22 h.

NPN-uptake measurements were performed after 2.5 h of selected treatment. 100 µL of the sample suspensions (per 3 replicates) were transferred in a black polystyrene 96-well flat bottom microplate by adding five µM of NPN. The relative intensity of fluorescence (excitation 350 nm, emission 460 nm) was instantly measured with TECAN GENios Pro^{TM} (Männedorf, Switzerland) plate reader. The plate was shaken 5 s before each registration point. The 1-NPN cell uptake factor was calculated as a ratio between the intensity of fluorescence values of the treated bacterial suspension and control samples without irradiation.

To evaluate the changes in antibiotic sensitivity of bacteria after exposure to MP, we used the Microdilution Checkerboard Method. The minimal inhibitory concentration (MIC) is the amount of antibiotic required to reduce bacterial growth by 50 (MIC50) and 90 percent, respectively (MIC90). After irradiation, 1 ml of the suspension was removed from the cuvettes and used to determine MIC values. First, 96-well transparent plates were filled with LB-medium broth (Roth, Germany). The maximal antibiotic concentrations of

tetracycline and chloramphenicol were 4 μg/mL and 16 μg/mL respectively. Two-fold dilutions were performed. Then, 50 μL of treated bacteria suspensions were inoculated (about 1.5 × 103 cfu/mL). The total amount of suspension was 200 μL per well. The absorption was measured with TECAN GENios Pro™ (Männedorf, Switzerland) multifunction plate reader at 612 nm after 24 h of incubation without agitation under 37 °C temperature (Memmert, Germany).

4. Conclusions

In the current study, bi-layered magnetic photocatalyst powder consisting of a Ni layer on one side and carbon-doped TiO_2 or ZnO photocatalyst layers on the other side were synthesized by magnetron sputtering technique. Structural characterization of powders confirmed that in general, the applied method allowed the achievement of all implied properties of photocatalyst layers. More specifically, the TiO_2 layer was successfully doped by carbon to approximately 3 at. % which is beneficial for visible light photocatalysis. On the other hand, by synthesizing the ZnO layer, we managed to create a considerable number of intrinsic defects, which are also useful for visible light photocatalysis. By applying magnetic photocatalyst powder for the bleaching of MB and RhB solutions under UV and visible light, we observed that C-TiO_2+Ni was capable of nearly fully reducing both dyes. However, the efficiency of ZnO+MP was considerably lower and was deteriorating throughout five consecutive bleaching cycles.

Photocatalyst performance tests with live *Salmonella* Typhimurium bacteria showed that neither of the two magnetic photocatalyst powders was capable of fully disinfecting the bacteria. On one hand, this was attributed to the insufficient permeabilization of the *S.* Typhimurium cell membrane. On the other hand, zinc dissolution was also considered a significant factor. Interestingly, even when photocatalytic treatment was relatively meager, bacteria still suffered significant damage and were considerably more vulnerable to antibiotics, especially for tetracycline.

Author Contributions: Conceptualization and methodology, M.L., S.V., M.U., S.S. and R.D.; investigation, S.T., S.V., M.U., S.S.; writing—original draft preparation, M.L., S.T. and S.S.; writing—review and editing, M.L., S.V. and M.U.; visualization, S.T. and M.L. All authors have read and agreed to the published version of the manuscript.

Funding: This research is funded by the European Social Fund according to the activity "Improvement of researchers" qualification by implementing world-class R&D projects of Measure No. 09.3.3-LMT-K-712, project "Investigation of the application of TiO_2 and ZnO for the visible light assisted photocatalytic disinfection of biologically contaminated water" (09.3.3-LMT-K-712-01-0175).

Data Availability Statement: Not applicable.

Acknowledgments: The authors express gratitude to Neringa Kuliesiene for her valuable input in the conceptualization and interpretation of experimental results; Mindaugas Aikas, Rolandas Uscila, Emilija Demikyte, and Deimante Vasiliauske for their input in the preparation of the samples and testing facilities.

Conflicts of Interest: The authors declare no conflict of interest.

References

1. UNESCO World Water Assessment Programme. *The United Nations World Water Development Report 2020: Water and Climate Change*; UNESCO: Paris, France, 2020.
2. UNESCO World Water Assessment Programme. *The United Nations World Water Development Report 2021: Valuing Water*; UNESCO: Paris, France, 2021.
3. UNESCO World Water Assessment Programme. *The United Nations World Water Development Report 2022: Groundwater: Making the Invisible Visible*; UNESCO: Paris, France, 2022.
4. Reznik, A.; Dinar, A.; Hernández-Sancho, F. Treated Wastewater Reuse: An Efficient and Sustainable Solution for Water Resource Scarcity. *Environ. Resour. Econ.* **2019**, *74*, 1647–1685. [CrossRef]

5. Faragò, M.; Damgaard, A.; Madsen, J.A.; Andersen, J.K.; Thornberg, D.; Andersen, M.H.; Rygaard, M. From wastewater treatment to water resource recovery: Environmental and economic impacts of full-scale implementation. *Water Res.* **2021**, *204*, 117554. [CrossRef] [PubMed]
6. Crosson, C.; Tong, D.; Zhang, Y.; Zhong, Q. Rainwater as a renewable resource to achieve net zero urban water in water stressed cities. *Resour. Conserv. Recycl.* **2021**, *164*, 105203. [CrossRef]
7. Huang, Z.; Nya, E.L.; Rahman, M.A.; Mwamila, T.B.; Cao, V.; Gwenzi, W.; Noubactep, C. Integrated Water Resource Management: Rethinking the Contribution of Rainwater Harvesting. *Sustainability* **2021**, *13*, 8338. [CrossRef]
8. Rahaman, M.F.; Jahan, C.S.; Mazumder, Q.H. Rainwater harvesting: Practiced potential for Integrated Water Resource Management in drought-prone Barind Tract, Bangladesh. *Groundw. Sustain. Dev.* **2019**, *9*, 100267. [CrossRef]
9. Ding, X.; Cai, Z.; Fu, Z. Does the new-type urbanization construction improve the efficiency of agricultural green water utilization in the Yangtze River Economic Belt? *Environ. Sci. Pollut. Res.* **2021**, *28*, 64103–64112. [CrossRef]
10. Paumo, H.K.; Dalhatou, S.; Katata-Seru, L.M.; Kamdem, B.P.; Tijani, J.O.; Vishwanathan, V.; Kane, A.; Bahadur, I. TiO_2 assisted photocatalysts for degradation of emerging organic pollutants in water and wastewater. *J. Mol. Liq.* **2021**, *331*, 115458. [CrossRef]
11. Zhang, C.; Xu, L.; Mou, X.; Xu, H.; Liu, J.; Miao, Y.; Wang, X.C.; Li, X. Characterization and evolution of antibiotic resistance of Salmonella in municipal wastewater treatment plants. *J. Environ. Manag.* **2019**, *251*, 109547. [CrossRef]
12. Al-Abri, M.; Al-Ghafri, B.; Bora, T.; Dobretsov, S.; Dutta, J.; Castelletto, S.; Rosa, L.; Boretti, A. Chlorination disadvantages and alternative routes for biofouling control in reverse osmosis desalination. *npj Clean Water* **2019**, *2*, 2. [CrossRef]
13. Pedahzur, R.; Katzenelson, D.; Barnea, N.; Lev, O.; Shuval, H.I.; Fattal, B.; Ulitzur, S. The efficacy of long-lasting residual drinking water disinfectants based on hydrogen peroxide and silver. *Water Sci. Technol.* **2000**, *42*, 293–298. [CrossRef]
14. Letifi, H.; Dridi, D.; Litaiem, Y.; Ammar, S.; Dimassi, W.; Chtourou, R. High Efficient and Cost Effective Titanium Doped Tin Dioxide Based Photocatalysts Synthesized via Co-precipitation Approach. *Catalysts* **2021**, *11*, 803. [CrossRef]
15. Ray, S.K.; Dhakal, D.; Regmi, C.; Yamaguchui, T.; Lee, S.W. Inactivation of Staphylococcus aureus in visible light by morphology tuned α-NiMoO4. *J. Photochem. Photobiol. A Chem.* **2018**, *350*, 59–68. [CrossRef]
16. García-Espinoza, J.D.; Robles, I.; Durán-Moreno, A.; Godínez, L.A. Photo-assisted electrochemical advanced oxidation processes for the disinfection of aqueous solutions: A review. *Chemosphere* **2021**, *274*, 129957. [CrossRef] [PubMed]
17. Du, Y.; Xiong, H.; Dong, S.; Zhang, J.; Ma, D.; Zhou, D. Identifying the role of reactive oxygen species (ROSs) in Fusarium solani spores inactivation. *AMB Express* **2016**, *6*, 81. [CrossRef]
18. Hasija, V.; Kumar, A.; Sudhaik, A.; Raizada, P.; Singh, P.; Van Le, Q.; Le, T.T.; Nguyen, V.-H. Step-scheme heterojunction photocatalysts for solar energy, water splitting, CO2 conversion, and bacterial inactivation: A review. *Environ. Chem. Lett.* **2021**, *19*, 2941–2966. [CrossRef]
19. Bhatkhande, D.S.; Pangarkar, V.G.; Beenackers, A.A.C.M. Photocatalytic degradation for environmental applications—A review. *J. Chem. Technol. Biotechnol.* **2002**, *77*, 102–116. [CrossRef]
20. Thongam, D.D.; Chaturvedi, H. Advances in nanomaterials for heterogeneous photocatalysis. *Nano Express* **2021**, *2*, 12005. [CrossRef]
21. Piątkowska, A.; Janus, M.; Szymański, K.; Mozia, S. C-,N- and S-Doped TiO2 Photocatalysts: A Review. *Catalysts* **2021**, *11*, 144. [CrossRef]
22. Lee, K.M.; Lai, C.W.; Ngai, K.S.; Juan, J.C. Recent developments of zinc oxide based photocatalyst in water treatment technology: A review. *Water Res.* **2016**, *88*, 428–448. [CrossRef]
23. Lofrano, G.; Ubaldi, F.; Albarano, L.; Carotenuto, M.; Vaiano, V.; Valeriani, F.; Libralato, G.; Gianfranceschi, G.; Fratoddi, I.; Meric, S.; et al. Antimicrobial Effectiveness of Innovative Photocatalysts: A Review. *Nanomaterials* **2022**, *12*, 2831. [CrossRef]
24. Gogoi, D.; Namdeo, A.; Golder, A.K.; Peela, N.R. Ag-doped TiO2 photocatalysts with effective charge transfer for highly efficient hydrogen production through water splitting. *Int. J. Hydrogen Energy* **2020**, *45*, 2729–2744. [CrossRef]
25. Mollavali, M.; Rohani, S.; Elahifard, M.; Behjatmanesh-Ardakani, R.; Nourany, M. Band gap reduction of (Mo+N) co-doped TiO2 nanotube arrays with a significant enhancement in visible light photo-conversion: A combination of experimental and theoretical study. *Int. J. Hydrogen Energy* **2021**, *46*, 21475–21498. [CrossRef]
26. Bakar, S.A.; Ribeiro, C. Nitrogen-doped titanium dioxide: An overview of material design and dimensionality effect over modern applications. *J. Photochem. Photobiol. C Photochem. Rev.* **2016**, *27*, 1–29. [CrossRef]
27. Changanaqui, K.; Brillas, E.; Alarcón, H.; Sirés, I. ZnO/TiO2/Ag2Se nanostructures as photoelectrocatalysts for the degradation of oxytetracycline in water. *Electrochim. Acta* **2020**, *331*, 135194. [CrossRef]
28. Hunger, M.; Hüsken, G.; Brouwers, H.J.H. Photocatalytic degradation of air pollutants—From modeling to large scale application. *Cem. Concr. Res.* **2010**, *40*, 313–320. [CrossRef]
29. Tang, T.; Yin, Z.; Chen, J.; Zhang, S.; Sheng, W.; Wei, W.; Xiao, Y.; Shi, Q.; Cao, S. Novel p-n heterojunction Bi2O3/Ti3+-TiO2 photocatalyst enables the complete removal of tetracyclines under visible light. *Chem. Eng. J.* **2021**, *417*, 128058. [CrossRef]
30. Yu, J.; Low, J.; Xiao, W.; Zhou, P.; Jaroniec, M. Enhanced Photocatalytic CO2-Reduction Activity of Anatase TiO2 by Coexposed {001} and {101} Facets. *J. Am. Chem. Soc.* **2014**, *136*, 8839–8842. [CrossRef]
31. Ong, W.-J.; Tan, L.-L.; Chai, S.-P.; Yong, S.-T.; Mohamed, A.R. Highly reactive {001} facets of TiO2-based composites: Synthesis, formation mechanism and characterization. *Nanoscale* **2014**, *6*, 1946–2008. [CrossRef]
32. Xu, Q.; Zhang, L.; Yu, J.; Wageh, S.; Al-Ghamdi, A.A.; Jaroniec, M. Direct Z-scheme photocatalysts: Principles, synthesis, and applications. *Mater. Today* **2018**, *21*, 1042–1063. [CrossRef]

33. Wang, J.; Wang, G.; Cheng, B.; Yu, J.; Fan, J. Sulfur-doped g-C3N4/TiO2 S-scheme heterojunction photocatalyst for Congo Red photodegradation. *Chin. J. Catal.* **2021**, *42*, 56–68. [CrossRef]
34. Fu, J.; Xu, Q.; Low, J.; Jiang, C.; Yu, J. Ultrathin 2D/2D WO3/g-C3N4 step-scheme H2-production photocatalyst. *Appl. Catal. B Environ.* **2019**, *243*, 556–565. [CrossRef]
35. Feng, X.; Yu, Z.; Sun, Y.; Shan, M.; Long, R.; Li, X. 3D MXene/Ag2S material as Schottky junction catalyst with stable and enhanced photocatalytic activity and photocorrosion resistance. *Sep. Purif. Technol.* **2021**, *266*, 118606. [CrossRef]
36. Li, W.; Chu, X.; He, S.; Wang, X.; Wang, C. A gourd-like hollow mesoporous silica particle-supported Ag/AgBr Schottky junction for highly efficient mineralization of tetracycline hydrochloride. *Environ. Sci. Nano* **2020**, *7*, 2654–2668. [CrossRef]
37. Ivanova, I.; Schneider, J.; Gutzmann, H.; Kliemann, J.O.; Gärtner, F.; Klassen, T.; Bahnemann, D.; Mendive, C.B. Photocatalytic degradation of oxalic and dichloroacetic acid on TiO 2 coated metal substrates. *Catal. Today* **2013**, *209*, 84–90. [CrossRef]
38. Wenhua, L.; Hong, L.; Sao'an, C.; Jianqing, Z.; Chunan, C. Kinetics of photocatalytic degradation of aniline in water over TiO2 supported on porous nickel. *J. Photochem. Photobiol. A Chem.* **2000**, *131*, 125–132. [CrossRef]
39. Liu, Y.; Zhu, X.; Yuan, D.; Wang, W.; Gao, L. Preparation and characterization of TiO2 based on wood templates. *Sci. Rep.* **2020**, *10*, 12444. [CrossRef]
40. Hu, X.; Hu, X.; Tang, C.; Wen, S.; Wu, X.; Long, J.; Yang, X.; Wang, H.; Zhou, L. Mechanisms underlying degradation pathways of microcystin-LR with doped TiO2 photocatalysis. *Chem. Eng. J.* **2017**, *330*, 355–371. [CrossRef]
41. Li, Y.-F.; Liu, Z.-P. Particle Size, Shape and Activity for Photocatalysis on Titania Anatase Nanoparticles in Aqueous Surroundings. *J. Am. Chem. Soc.* **2011**, *133*, 15743–15752. [CrossRef]
42. Mirzaeifard, Z.; Shariatinia, Z.; Jourshabani, M.; Rezaei Darvishi, S.M. ZnO Photocatalyst Revisited: Effective Photocatalytic Degradation of Emerging Contaminants Using S-Doped ZnO Nanoparticles under Visible Light Radiation. *Ind. Eng. Chem. Res.* **2020**, *59*, 15894–15911. [CrossRef]
43. Xiu, Z.; Guo, M.; Zhao, T.; Pan, K.; Xing, Z.; Li, Z.; Zhou, W. Recent advances in Ti^{3+} self-doped nanostructured TiO_2 visible light photocatalysts for environmental and energy applications. *Chem. Eng. J.* **2020**, *382*, 123011. [CrossRef]
44. Ruiz-Aguirre, A.; Villachica-Llamosas, J.G.; Polo-López, M.I.; Cabrera-Reina, A.; Colón, G.; Peral, J.; Malato, S. Assessment of pilot-plant scale solar photocatalytic hydrogen generation with multiple approaches: Valorization, water decontamination and disinfection. *Energy* **2022**, *260*, 125199. [CrossRef]
45. Veréb, G.; Hernádi, K.; Baia, L.; Rákhely, G.; Pap, Z. Chapter 12—Pilot-plant scaled water treatment technologies, standards for the removal of contaminants of emerging concern based on photocatalytic materials. In *Micro and Nano Technologies*; Baia, L., Pap, Z., Hernadi, K., Baia, M., Eds.; Elsevier: Amsterdam, The Netherlands, 2020; pp. 493–523.
46. Shan, A.Y.; Ghazi, T.I.M.; Rashid, S.A. Immobilisation of titanium dioxide onto supporting materials in heterogeneous photocatalysis: A review. *Appl. Catal. A Gen.* **2010**, *389*, 1–8. [CrossRef]
47. Srikanth, B.; Goutham, R.; Badri Narayan, R.; Ramprasath, A.; Gopinath, K.P.; Sankaranarayanan, A.R. Recent advancements in supporting materials for immobilised photocatalytic applications in waste water treatment. *J. Environ. Manag.* **2017**, *200*, 60–78. [CrossRef] [PubMed]
48. Beydoun, D.; Amal, R.; Low, G.K.-C.; McEvoy, S. Novel Photocatalyst: Titania-Coated Magnetite. Activity and Photodissolution. *J. Phys. Chem. B* **2000**, *104*, 4387–4396. [CrossRef]
49. Beydoun, D.; Amal, R. Implications of heat treatment on the properties of a magnetic iron oxide–titanium dioxide photocatalyst. *Mater. Sci. Eng. B* **2002**, *94*, 71–81. [CrossRef]
50. Jacinto, M.J.; Ferreira, L.F.; Silva, V.C. Magnetic materials for photocatalytic applications—A review. *J. Sol-Gel Sci. Technol.* **2020**, *96*, 1–14. [CrossRef]
51. Elgohary, E.A.; Mohamed, Y.M.A.; El Nazer, H.A.; Baaloudj, O.; Alyami, M.S.S.; El Jery, A.; Assadi, A.A.; Amrane, A. A Review of the Use of Semiconductors as Catalysts in the Photocatalytic Inactivation of Microorganisms. *Catalysts* **2021**, *11*, 1498. [CrossRef]
52. Varnagiris, S.; Urbonavičius, M.; Sakalauskaitė, S.; Demikyte, E.; Tuckute, S. Floating Carbon-Doped TiO2 Photocatalyst with Metallic Underlayers Investigation for Polluted Water Treatment under Visible-Light Irradiation. *Catalysts* **2021**, *11*, 1454. [CrossRef]
53. Sakalauskaite, S.; Vasiliauske, D.; Demikyte, E.; Daugelavicius, R.; Lelis, M. Influence of the Metabolic Activity of Microorganisms on Disinfection Efficiency of the Visible Light and P25 TiO2 Photocatalyst. *Catalysts* **2021**, *11*, 1432. [CrossRef]
54. Restifo, L.L.; Vogelbacker, H.H.; Madara, T.; Ling, S.K.; Kozinski, A.W. Effects of UV irradiation on the fate of 5-bromodeoxyuridine-substituted bacteriophage T4 DNA. *J. Virol.* **1983**, *47*, 151–170. [CrossRef]
55. Ellmer, K. Magnetron sputtering of transparent conductive zinc oxide: Relation between the sputtering parameters and the electronic properties. *J. Phys. D Appl. Phys.* **2000**, *33*, R17–R32. [CrossRef]
56. Tučkutė, S.; Urbonavičius, M.; Lelis, M.; Maiorov, M.; Ordaz, J.R.D.; Milčius, D. A new method of nanocrystalline nickel powder formation by magnetron sputtering on the water-soluble substrates. *Mater. Res. Express* **2018**, *5*, 015017. [CrossRef]
57. Varnagiris, S.; Medvids, A.; Lelis, M.; Milcius, D.; Antuzevics, A. Black carbon-doped TiO2 films: Synthesis, characterization and photocatalysis. *J. Photochem. Photobiol. A Chem.* **2019**, *382*, 111941. [CrossRef]
58. Lelis, M.; Varnagiris, S.; Urbonavicius, M.; Zakarauskas, K. Investigation of Catalyst Development from Mg2NiH4 Hydride and Its Application for the CO2 Methanation Reaction. *Coatings* **2020**, *10*, 1178. [CrossRef]

59. Bockute, K.; Demikyte, E.; Tuckute, S.; Urbonavičius, M.; Varnagiris, S.; Laukaitis, G.; Lelis, M. Photoluminescence and structural defects of ZnO films deposited by reactive magnetron sputtering with unconventional Ar-O2 gas mixture formation. In Proceedings of the SurfCoat Korea 2021, Online, 26–28 May 2021; pp. 2–8.
60. Wu, H.; Ma, J.; Zhang, C.; He, H. Effect of TiO2 calcination temperature on the photocatalytic oxidation of gaseous NH3. *J. Environ. Sci.* **2014**, *26*, 673–682. [CrossRef] [PubMed]
61. Sienkiewicz, A.; Wanag, A.; Kusiak-Nejman, E.; Ekiert, E.; Rokicka-Konieczna, P.; Morawski, A.W. Effect of calcination on the photocatalytic activity and stability of TiO2 photocatalysts modified with APTES. *J. Environ. Chem. Eng.* **2021**, *9*, 104794. [CrossRef]
62. Andia-Huaracha, S.C.; Zapana-Cayo, L.M.; Aragón, F.F.H.; Aquino, J.C.R.; Coaquira, J.A.H.; Gonzales-Lorenzo, C.D.; Ayala-Arenas, J.S.; Solis, J.L.; Morais, P.C.; Pacheco-Salazar, D.G. Tuning the photocatalytic activity of ZnO nanoparticles by the annihilation of intrinsic defects provoked by the thermal annealing. *J. Nanopart. Res.* **2022**, *24*, 50. [CrossRef]
63. Springthorpe, A.J. The Rhombohedral Distortion in NiO. In *Physica Status Solidi*; Gutsche, E., Müller, K., Görlich, P., Eds.; De Gruyter: Berlin, Germany; Boston, MA, USA, 1967; pp. 399–400.
64. He, G.; Zhang, H.; Ni, J.; Liu, B.; Xu, C.; Xiang, H. Microscopic Magnetic Origin of Rhombohedral Distortion in NiO. *Chin. Phys. Lett.* **2022**, *39*, 67501. [CrossRef]
65. Hotovy, I.; Huran, J.; Spiess, L. Characterization of sputtered NiO films using XRD and AFM. *J. Mater. Sci.* **2004**, *39*, 2609–2612. [CrossRef]
66. Zhang, L.; Tse, M.S.; Tan, O.K.; Wang, Y.X.; Han, M. Facile fabrication and characterization of multi-type carbon-doped TiO2 for visible light-activated photocatalytic mineralization of gaseous toluene. *J. Mater. Chem. A* **2013**, *1*, 4497–4507. [CrossRef]
67. Ząbek, P.; Eberl, J.; Kisch, H. On the origin of visible light activity in carbon-modified titania. *Photochem. Photobiol. Sci.* **2009**, *8*, 264–269. [CrossRef] [PubMed]
68. Chen, X.; Wang, X.; Fang, D. A review on C1s XPS-spectra for some kinds of carbon materials. *Fuller. Nanotub. Carbon Nanostruct.* **2020**, *28*, 1048–1058. [CrossRef]
69. Byrne, C.; Subramanian, G.; Pillai, S.C. Recent advances in photocatalysis for environmental applications. *J. Environ. Chem. Eng.* **2018**, *6*, 3531–3555. [CrossRef]
70. Ohno, T.; Tokieda, K.; Higashida, S.; Matsumura, M. Synergism between rutile and anatase TiO2 particles in photocatalytic oxidation of naphthalene. *Appl. Catal. A Gen.* **2003**, *244*, 383–391. [CrossRef]
71. Liu, H.; Yang, W.; Ma, Y.; Yao, J. Extended visible light response of binary TiO2-Ti 2O3 photocatalyst prepared by a photo-assisted sol-gel method. *Appl. Catal. A Gen.* **2006**, *299*, 218–223. [CrossRef]
72. Grabstanowicz, L.R.; Gao, S.; Li, T.; Rickard, R.M.; Rajh, T.; Liu, D.J.; Xu, T. Facile oxidative conversion of TiH2 to high-concentration Ti3+-self-doped rutile TiO2 with visible-light photoactivity. *Inorg. Chem.* **2013**, *52*, 3884–3890. [CrossRef]
73. Atla, S.B.; Chen, C.-C.; Chen, C.-Y.; Lin, P.-Y.; Pan, W.; Cheng, K.-C.; Huang, Y.M.; Chang, Y.-F.; Jean, J.-S. Visible light response of Ag+/TiO2–Ti2O3 prepared by photodeposition under foam fractionation. *J. Photochem. Photobiol. A Chem.* **2012**, *236*, 1–8. [CrossRef]
74. Yang, Y.; Ni, D.; Yao, Y.; Zhong, Y.; Ma, Y.; Yao, J. High photocatalytic activity of carbon doped TiO2 prepared by fast combustion of organic capping ligands. *RSC Adv.* **2015**, *5*, 93635–93643. [CrossRef]
75. Shao, J.; Sheng, W.; Wang, M.; Li, S.; Chen, J.; Zhang, Y.; Cao, S. In situ synthesis of carbon-doped TiO2 single-crystal nanorods with a remarkably photocatalytic efficiency. *Appl. Catal. B Environ.* **2017**, *209*, 311–319. [CrossRef]
76. Kunj, S.; Sreenivas, K. Residual stress and defect content in magnetron sputtered ZnO films grown on unheated glass substrates. *Curr. Appl. Phys.* **2016**, *16*, 748–756. [CrossRef]
77. Suo, X.; Zhao, S.; Ran, Y.; Liu, H.; Jiang, Z.; Li, Y.; Wang, Z. Effects of oxygen/argon pressure ratio on the structural and optical properties of Mn-doped ZnO thin films prepared by magnetron pulsed co-sputtering. *Surf. Coat. Technol.* **2019**, *357*, 978–983. [CrossRef]
78. Cicek, K.; Karacali, T.; Efeoglu, H.; Cakmak, B. Deposition of ZnO thin films by RF&DC magnetron sputtering on silicon and porous-silicon substrates for pyroelectric applications. *Sens. Actuators A Phys.* **2017**, *260*, 24–28.
79. Younas, R.; Afzal, N.; Rafique, M.; Imran, M.; Saleem, M.; Ahmad, R. Nickel ion implantation effects on DC magnetron sputtered ZnO film prepared on Si (100). *Ceram. Int.* **2019**, *45*, 15547–15555. [CrossRef]
80. Ievtushenko, A.I.; Karpyna, V.A.; Lazorenko, V.I.; Lashkarev, G.V.; Khranovskyy, V.D.; Baturin, V.A.; Karpenko, O.Y.; Lunika, M.M.; Avramenko, K.A.; Strelchuk, V.V.; et al. High quality ZnO films deposited by radio-frequency magnetron sputtering using layer by layer growth method. *Thin Solid Films* **2010**, *518*, 4529–4532. [CrossRef]
81. Wang, Y.; Chu, B. Structural and optical properties of ZnO thin films on (111) CaF2 substrates grown by magnetron sputtering. *Superlattices Microstruct.* **2008**, *44*, 54–61. [CrossRef]
82. Yau, W.-H.; Tseng, P.-C.; Lian, D. Nanoscratch study of ZnO thin films deposited using radio frequency magnetron sputtering. *Nucl. Instrum. Methods Phys. Res. Sect. B Beam Interact. Mater. Atoms* **2011**, *269*, 1450–1454. [CrossRef]
83. Vempati, S.; Mitra, J.; Dawson, P. One-step synthesis of ZnO nanosheets: A blue-white fluorophore. *Nanoscale Res. Lett.* **2012**, *7*, 470. [CrossRef]
84. Kayaci, F.; Vempati, S.; Donmez, I.; Biyikli, N.; Uyar, T. Role of zinc interstitials and oxygen vacancies of ZnO in photocatalysis: A bottom-up approach to control defect density. *Nanoscale* **2014**, *6*, 10224–10234. [CrossRef]

85. Urbonavicius, M.; Varnagiris, S.; Tuckute, S.; Sakalauskaite, S.; Demikyte, E.; Lelis, M. Visible-Light-Driven Photocatalytic Inactivation of Bacteria, Bacteriophages, and Their Mixtures Using ZnO-Coated HDPE Beads as Floating Photocatalyst. *Materials* **2022**, *15*, 1318. [CrossRef]
86. Mikami, M.; Eto, T.; Wang, J.; Masa, Y.; Isshiki, M. Growth of zinc oxide by chemical vapor transport. *J. Cryst. Growth* **2005**, *276*, 389–392. [CrossRef]
87. NIST. *X-ray Photoelectron Spectroscopy Database,* Version 4.1; NIST Standard Reference Database 20; NIST: Gaithersburg, MD, USA, 2012.
88. Abdel-Wahab, M.S.; Jilani, A.; Yahia, I.S.; Al-Ghamdi, A.A. Enhanced the photocatalytic activity of Ni-doped ZnO thin films: Morphological, optical and XPS analysis. *Superlattices Microstruct.* **2016**, *94*, 108–118. [CrossRef]
89. Guo, H.-L.; Zhu, Q.; Wu, X.-L.; Jiang, Y.-F.; Xie, X.; Xu, A.-W. Oxygen deficient ZnO1−x nanosheets with high visible light photocatalytic activity. *Nanoscale* **2015**, *7*, 7216–7223. [CrossRef] [PubMed]
90. Al-Gaashani, R.; Radiman, S.; Daud, A.R.; Tabet, N.; Al-Douri, Y. XPS and optical studies of different morphologies of ZnO nanostructures prepared by microwave methods. *Ceram. Int.* **2013**, *39*, 2283–2292. [CrossRef]
91. Verdier, T.; Coutand, M.; Bertron, A.; Roques, C. Antibacterial Activity of TiO2 Photocatalyst Alone or in Coatings on E. coli: The Influence of Methodological Aspects. *Coatings* **2014**, *4*, 670–686. [CrossRef]
92. Kumar, P.; Mathpal, M.C.; Inwati, G.K.; Ghosh, S.; Kumar, V.; Roos, W.D.; Swart, H.C. Optical and surface properties of Zn doped CdO nanorods and antimicrobial applications. *Colloids Surf. A Physicochem. Eng. Asp.* **2020**, *605*, 125369. [CrossRef]
93. Cataño, F.A.; Valencia, S.; Hincapié, E.A.; Restrepo, G.; Marín, J.M. A Comparative study between TiO2 and ZnO photocatalysis: Photocatalytic degradation of cibacron yellow FN-2R dye. *Lat. Am. Appl. Res.* **2012**, *42*, 33–38.
94. Li, Y.; Xie, S.; Xu, D.; Shu, G.; Wang, X. Antibacterial activity of ZnO quantum dots and its protective effects of chicks infected with Salmonella pullorum. *Nanotechnology* **2021**, *32*, 505104. [CrossRef]
95. Ye, X.J.; Zhong, W.; Xu, M.H.; Qi, X.S.; Au, C.T.; Du, Y.W. The magnetic property of carbon-doped TiO2. *Phys. Lett. A* **2009**, *373*, 3684–3687. [CrossRef]
96. Ablat, A.; Wu, R.; Mamat, M.; Ghupur, Y.; Aimidula, A.; Bake, M.A.; Gholam, T.; Wang, J.; Qian, H.; Wu, R.; et al. Electronic structure and room temperature ferromagnetism of C doped TiO2. *Solid State Commun.* **2016**, *243*, 7–11. [CrossRef]
97. Garcia, M.A.; Merino, J.M.; Fernández Pinel, E.; Quesada, A.; de la Venta, J.; Ruíz González, M.L.; Castro, G.R.; Crespo, P.; Llopis, J.; González-Calbet, J.M.; et al. Magnetic Properties of ZnO Nanoparticles. *Nano Lett.* **2007**, *7*, 1489–1494. [CrossRef]
98. Limón-Rocha, I.; Marizcal-Barba, A.; Guzmán-González, C.A.; Anaya-Esparza, L.M.; Ghotekar, S.; González-Vargas, O.A.; Pérez-Larios, A. Co, Cu, Fe, and Ni Deposited over TiO2 and Their Photocatalytic Activity in the Degradation of 2,4-Dichlorophenol and 2,4-Dichlorophenoxyacetic Acid. *Inorganics* **2022**, *10*, 157. [CrossRef]
99. Yeh, T.-S.; Wu, J.-M.; Hu, L.-J. The properties of TiN thin films deposited by pulsed direct current magnetron sputtering. *Thin Solid Films* **2008**, *516*, 7294–7298. [CrossRef]
100. Cooke, K.E.; Hampshire, J.; Southall, W.; Teer, D.G. Industrial Application of Pulsed Dc Bias Power Supplies in Closed Field Unbalanced Magnetron Sputter Ion Plating. *Surf. Eng.* **2004**, *20*, 189–195. [CrossRef]
101. Vlček, J.; Pajdarová, A.D.; Musil, J. Pulsed dc Magnetron Discharges and their Utilization in Plasma Surface Engineering. *Contrib. Plasma Phys.* **2004**, *44*, 426–436. [CrossRef]
102. Lelis, M.; Tuckute, S.; Urbonavicius, M.; Varnagiris, S.; Demikyte, E. Non-Conventional Synthesis and Repetitive Application of Magnetic Visible Light Photocatalyst Powder Consisting of Bi-Layered C-Doped TiO2 and Ni Particles. *Catalysts* **2023**, *13*, 169. [CrossRef]